Supplement for "Electrically interfaced Brillouin-active waveguide for microwave photonic measurements"

1. DYNAMICS OF ELECTRICALLY INTERFACED BRILLOUIN-ACTIVE WAVEGUIDE

In this section, we describe a simple model that captures the mode evolution dynamics of our electrically interfaced Brillouin-active waveguide. We will start with the Hamiltonian $\mathcal{H} = \mathcal{H}_{\rm opt} + \mathcal{H}_{\rm ph} + \mathcal{H}_{\rm int}$ for forward Brillouin scattering process [1, 2], given as

$$g\mathcal{H}_{\rm opt} = \sum_{\gamma} \int \mathrm{d}k \hbar\omega(k) a^{\dagger}_{\gamma k} a_{\gamma k}, \tag{S1}$$

$$\mathcal{H}_{\rm ph} = \sum_{\alpha} \int \mathrm{d}q \hbar\Omega(q) b^{\dagger}_{\alpha q} b_{\alpha q}, \tag{S2}$$

$$\mathcal{H}_{\rm int} = \sum_{\alpha,\gamma,\gamma'} \int \frac{\mathrm{d}k \mathrm{d}k' \mathrm{d}q}{(2\pi)^{3/2}} a^{\dagger}_{\gamma k} a_{\gamma' k'} b_{\alpha q} \int \mathrm{d}z \hbar g(\gamma k; \gamma' k'; \alpha q) e^{i(k'-k+q)z} + \text{H.c.}. \tag{S3}$$

Here, $b_{\alpha q}$ and $a_{\gamma k}$ represent the acoustic-mode amplitude operator and the optical amplitude operator. γ, γ', and α represent the optical and phonon mode indices, with wave vectors k, k', and q, respectively. In our intramodal Brillouin scattering system, we consider a single optical TE0 mode and a single acoustic membrane Lamb-like mode, which allows for a simplification of the mode indices summation. Additionally, the coupling rate $g(\gamma k; \gamma' k'; \alpha q)$ can be regarded as constant within a reasonable wavelength range in our low optical dispersion system, such that $g = g(\gamma k; \gamma' k'; \alpha q)$. Consequently, we can simplify the Hamiltonian as

$$\mathcal{H} = \int \mathrm{d}k \hbar\omega(k) a^{\dagger}_{k} a_{k} + \int \mathrm{d}q \hbar\Omega(q) b^{\dagger}_{q} b_{q} + \hbar g \int \frac{\mathrm{d}k \mathrm{d}q}{\sqrt{2\pi}} a^{\dagger}_{k} a_{k-q} \left(b_{q} + b^{\dagger}_{-q} \right). \tag{S4}$$

To describe the dynamics of a wideband optical envelope that might span several Stokes shifts, we transform to the spatial domain by introducing envelope operators $a(z,t)$ and $b(z,t)$

$$a(z,t) = \int \frac{\mathrm{d}k}{\sqrt{2\pi}} a_{k} e^{ikz}, \quad b(z,t) = \int \frac{\mathrm{d}q}{\sqrt{2\pi}} b_{q} e^{iqz}. \tag{S5}$$

As a result, the optical (acoustic) power flow in the waveguide is written as $P^{\rm opt} = \hbar\omega_0 v_{\rm g} a^{\dagger}(z,t) a(z,t)$ ($P^{\rm ph} = \hbar\Omega_0 v_{\rm g,b} b^{\dagger}(z,t) b(z,t)$), where $v_{\rm g}$ ($v_{\rm g,b}$) is the group velocity of the photons (phonons).

In addition, we introduce the propagation operators $\mathcal{L}_a$ and $\mathcal{L}_b$ to describe the spatial domain Hamiltonian [3],

$$\mathcal{L}_a = \hbar\omega_0 + \hbar \sum_{n=1}^{\infty} \frac{(-i)^n}{n!} \frac{\partial^n \omega}{\partial k^n}\bigg|_{k_0} (\partial_z - ik_0)^n, \quad \mathcal{L}_b = \hbar\Omega_0 + \hbar \sum_{n=1}^{\infty} \frac{(-i)^n}{n!} \frac{\partial^n \Omega}{\partial q^n}\bigg|_{q} (\partial_z - iq)^n, \tag{S6}$$

where we assume that all optical carriers have the same frequency ω_0 because the modulation signal, even if it can be wideband, should have a frequency that is at least 10^{-7} smaller than the optical frequency. Therefore, the Hamiltonian of the Brillouin scattering process described using the spatial operators is

$$\mathcal{H} = \int \mathrm{d}z a^{\dagger}(z,t) \mathcal{L}_a a(z,t) + \int \mathrm{d}z b^{\dagger}(z,t) \mathcal{L}_b b(z,t) + g \int \mathrm{d}z a^{\dagger}(z,t) a(z,t) \left[b(z,t) + b^{\dagger}(z,t) \right]. \tag{S7}$$

This Hamiltonian is reminiscent of cavity optomechanical systems operating in the zero-detuning regime, where both the blue sideband and the red sideband are present in the system [4]. In this system, the mechanical displacement induces a phase shift on the light field, while leaving the optical amplitude unchanged. Similarly, in our waveguide, the intensity envelope of the photons, with its change described by

$$(\partial_t - v_{\rm g} \partial_z) \left(a^{\dagger} a \right) = 0, \tag{S8}$$

also remains time-independent during the scattering process. This similarity draws an analogy between our amplitude-preserving method and non-demolition measurements in cavity-optomechanics experiments.

The same conclusion can be verified by directly solving the equations of motion for photons and phonons, which are given as

$$\left(\partial_t + v_\mathrm{g}\partial_z\right)\tilde{a} = -ig\left(\tilde{b} + \tilde{b}^\dagger\right)\tilde{a}, \tag{S9}$$

$$\left[\partial_t - i(\Omega - \Omega_0) + \frac{\Gamma_0}{2}\right]\tilde{b} = -ig\tilde{a}^\dagger\tilde{a} + \sqrt{\xi}B_\mathrm{in}, \tag{S10}$$

where the rotating frame operators are introduced as $\tilde{a} = a\exp(i\omega_0 t - ik_0 z)$ and $\tilde{b} = b\exp(i\Omega t - iqz)$ to eliminate both the temporal and spatial carriers. Γ_0 and Ω_0 respectively represent the temporal power decay rate and the eigenfrequency of the phonon field. To simplify these equations, several assumptions are introduced: (1) The optical propagation operator is reduced to the first order due to the linear optical dispersion of our waveguide; (2) The acoustic propagation operator is simplified to the zeroth order owing to the negligible acoustic group velocity $v_{\mathrm{g,b}}$; (3) The optical propagation loss is disregarded within the system, considering the excellent low-loss characteristic of our waveguide and the short interaction region in our design. The right-hand-side of eq. (S10) contains two terms. The term $-ig\tilde{a}^\dagger\tilde{a}$ denotes the optical drive from stimulated Brillouin scattering, and the term $\sqrt{\xi}B_\mathrm{in}$ represents the microwave drive for the phonon field. The latter is determined by the extrinsic coupling rate ξ (with unit [Hz]) and the length-normalized electromechanical drive amplitude B_in (with unit [$\sqrt{\mathrm{Hz/m}}$]).

The initial conditions of our system are set to be

$$\tilde{a}(z = 0, t) = \tilde{a}_\mathrm{in}(t), \tag{S11}$$

where $\tilde{a}_\mathrm{in}$ is the incident optical envelope of our system. In the following text, we will discuss two separate situations in which either the optical drive or the microwave drive dominates the acoustic behaviors.

A. Optical phase modulator

In Fig. 2, we introduce an optical phase modulator where the incident signal is a monochromatic light field with a frequency ω_0 and an amplitude a_0, i.e. $\tilde{a}_\mathrm{in}(t) = a_0$. In this case, the phonon dynamics are primarily governed by the electromechanical drive, leading to the equation of motion for phonons

$$\frac{\partial\tilde{b}}{\partial t} + \chi_\mathrm{b}^{-1}(\Omega)\tilde{b} = \sqrt{\xi}B_\mathrm{in}, \tag{S12}$$

where we introduce the phonon susceptibility as $\chi_\mathrm{b}(\Omega) = \left[-i(\Omega - \Omega_0) + \Gamma_0/2\right]^{-1}$. In the steady-state approximation, the phonon amplitude is directly calculated as $b = \sqrt{\xi}\chi_\mathrm{b}B_\mathrm{in}$. Furthermore, using the input-output theory, we can obtain the electromechanical output of the acoustic drive, $B_\mathrm{out} = \sqrt{\xi}b = \xi\chi_\mathrm{b}B_\mathrm{in}$. Note that both B_in and B_out are directly transformed from or into microwave power input $P_\mathrm{RF}^\mathrm{in}$ and output $P_\mathrm{RF}^\mathrm{out}$ through the IDTs, with the transformation relationship expressed as

$$P_\mathrm{RF}^\mathrm{in} = \hbar\Omega L\left|B_\mathrm{in}(\Omega)\right|^2/\eta_\mathrm{e};\ P_\mathrm{RF}^\mathrm{out} = \hbar\Omega L\left|B_\mathrm{out}(\Omega)\right|^2\cdot\eta_\mathrm{e}. \tag{S13}$$

Here, L is the length of our electrically interfaced Brillouin-active waveguide. The microwave extinction, defined as $\eta_\mathrm{e} = 1 - \left|S_{11}(\Omega)\right|^2$, quantifies the efficiency of on-chip microwave coupling and is determined by the impedance design of the interdigital transducers (IDTs). In our experiments, we measure $|S_{11}(\Omega)|$ as the microwave reflection from a single IDT.

Correspondingly, the electromechanical coupling coefficient, which quantifies the power conversion efficiency from microwave to phonons, can be calculated as $\eta_\mathrm{em} = \sqrt{P_\mathrm{RF}^\mathrm{out}/P_\mathrm{RF}^\mathrm{in}}$. In our experiment, this coupling efficiency is measured as the microwave transmission $|S_{21}|$ from one IDT to the other. When the microwave drive is on resonance, we obtain $\eta_\mathrm{em} = |S_{21}| = \eta_\mathrm{e}\cdot 2\xi/\Gamma_0$. The second factor of this parameter represents the on-chip microwave-to-acoustic conversion efficiency, and in our paper, we denote it as $\eta_\mathrm{m} = 2\xi/\Gamma_0$.

Next, we study the optical dynamics of this system. Plugging in the constant amplitude of the phonon field into eq. (S9), we arrive at

$$\left(\frac{\partial}{\partial t} + v_\mathrm{g}\frac{\partial}{\partial z}\right)\tilde{a} = -i2g|b|\cos\left(\Omega_0 t\right)\tilde{a}, \tag{S14}$$

By solving this equation, we can analyze the output light at position z

$$\tilde{a}(z,t) = a_0\exp\left\{\frac{i2g|b|}{\Omega_0}\left\{\sin\left[\Omega_0\left(t - \frac{z}{v_\mathrm{g}}\right)\right] - \sin\left(\Omega_0 t\right)\right\}\right\}. \tag{S15}$$

In our system, $\Omega_0 z/v_{\mathrm{g}} \ll 1$ given the short interaction length of our device ($z < 160$ µm), the solution can be further simplified as a pure phase modulation

$$\tilde{a}(z,t) = a_0 \exp\left[-i\frac{2g|b|z}{v_{\mathrm{g}}}\cos(\Omega_0 t)\right]. \tag{S16}$$

This is how we derived eq. (1) and obtained the value for modulation depth, $\beta = 2g|b|z/v_{\mathrm{g}}$, as presented in the main text. In our experiment, we measure and analyze the phase-modulated output light by decomposing it into a series of distinct optical tones, each with a frequency $\omega_n = \omega_0 + n\Omega_0$. The amplitude of n-th sideband at position z can be obtained using Jacobi-Anger expansion, $e^{iz\cos\phi} = \sum_n i^n J_n(z) e^{in\phi}$. Hence we arrive at

$$\tilde{a}_n(z,t) = i^n a_0 J_n\left(-\frac{2g|b|z}{v_{\mathrm{g}}}\right) e^{-in\Omega_0 t}. \tag{S17}$$

Notice that the same dynamics can be derived using the cascading equations of motion for the traveling Brillouin scattering process [1, 5].

Combining eq.(S13) and (S17), we obtain the modulation depth on acoustic resonance

$$\beta = \sqrt{2\eta_{\mathrm{em}} G_{\mathrm{B}} P_{\mathrm{RF}} L}\sqrt{\frac{\omega_0}{\Omega_0}}, \tag{S18}$$

where we introduce the Brillouin gain coefficient $G_{\mathrm{B}} = 4g^2/(v_{\mathrm{g}}^2 \Gamma_0 \hbar\omega_0)$ [1] to simplify the expression. When using a microwave input with a standard impedance of $R_0 = 50\ \Omega$ to drive our system, the half-wave voltage V_π of this phase modulation can be directly obtained from the modulation depth β as

$$V_\pi = \pi\sqrt{\frac{R_0\Omega_0}{2\eta_{\mathrm{em}} G_{\mathrm{B}} L\omega_0}}. \tag{S19}$$

We can conclude that a higher electromechanical ($\propto \eta_{\mathrm{em}}$) or optomechanical ($\propto G_{\mathrm{B}}$) transduction rate, as well as a longer interaction length L, all contribute to a more efficient phase shifter.

When using this phase modulation for microwave-to-optical conversion, a small RF drive will be converted into ± 1 sidebands in the system. The flux of generated photons in one sideband, $R_{\mathrm{o}} = |a_{\pm 1}|^2 v_{\mathrm{g}}$, can then be obtained by expanding the Bessel function to first order $J_1(x) \approx x/2$, which is given as

$$R_{\mathrm{o}} = \frac{1}{2}\eta_{\mathrm{em}} G_{\mathrm{B}} P_{\mathrm{RF}} L \frac{\omega_0}{\Omega_0}|a_0|^2 v_{\mathrm{g}} = \frac{1}{2}\eta_{\mathrm{em}} G_{\mathrm{B}} P_0 L \frac{P_{\mathrm{RF}}}{\hbar\Omega_0}, \tag{S20}$$

where we calculate the optical pump power as $P_0 = \hbar\omega_0 v_{\mathrm{g}}|a_0|^2$. The flux of microwave photons R_{RF} that participate in this electo-optomechanical interaction can be calculated from the incident RF power P_{RF}, given as $R_{\mathrm{RF}} = P_{\mathrm{RF}}/(\hbar\Omega)$. Therefore the microwave-to-optical quantum conversion efficiency can then be obtained as

$$\eta = \frac{R_{\mathrm{o}}}{R_{\mathrm{RF}}} = \frac{1}{2}\eta_{\mathrm{em}} G_{\mathrm{B}} P_0 L. \tag{S21}$$

B. Optical-to-microwave transduction

This section focuses on the behavior of phonons driven solely by optical drives, as described by the equation

$$\frac{\partial\tilde{b}}{\partial t} + \chi_{\mathrm{b}}^{-1}(\Omega)\tilde{b} = -ig\tilde{a}^\dagger(z,t)\tilde{a}(z,t). \tag{S22}$$

In combination with eq. (S9), we arrive at the optical envelope solution [3]

$$\tilde{a}(z,t) = \tilde{a}_{\mathrm{in}}\left(t - \frac{z}{v_{\mathrm{g}}}\right)\exp\left\{-i2g\int \mathrm{d}z' \,\mathrm{Re}\left[\tilde{b}\left(z', t - \frac{z-z'}{v_{\mathrm{g}}}\right)\right]\right\}, \tag{S23}$$

which features a purely real-valued integrand, implying that it introduces only a phase modulation. Consequently, $\tilde{a}^\dagger(z,t)\tilde{a}(z,t) = \tilde{a}_{\mathrm{in}}^\dagger\tilde{a}_{\mathrm{in}}$, indicating that the envelope remains constant as the system evolves. This result is in accordance with the conclusion derived from the Hamiltonian discussion. In the subsequent discussions, we utilize this result to analyze two distinct experiments described in the paper: the characterization of transduction efficiency and the measurement of microwave channelization.

1. Two-tone excitation

In the transduction efficiency characterization experiment, we inject two optical drive fields, each with the frequency ω_0 (ω_{-1}) and amplitude a_0 (a_{-1}) into the system. Considering the rotating wave approximation, the stationary solution of the phonon field is then obtained as

$$\tilde{b} = -ig\chi_{\mathrm{b}}(\Omega)a_0(0)^\dagger a_{-1}(0). \tag{S24}$$

Following the electromechanical transduction process described in eq. (S13), the microwave output on acoustic resonance is calculated as $P_{\mathrm{RF}}^{\mathrm{out}} = \frac{1}{2}\eta_{\mathrm{em}}G_{\mathrm{B}}P_0L\hbar\Omega_0 v_{\mathrm{g}}|a_{-1}|^2$. Accordingly, the quantum efficiency of optical-to-microwave conversion is then

$$\eta = \frac{R_{\mathrm{RF}}}{R_{\mathrm{o}}} = \frac{1}{2}\eta_{\mathrm{em}}G_{\mathrm{B}}P_0L, \tag{S25}$$

which is consistent with our result of the microwave-to-optical conversion, as expected.

2. Intensity-modulated light input

For the channelization experiment, we inject an intensity-modulated optical field into the system. We first consider the single-segment case, where the modulation signal is a single-frequency tone with the modulation frequency Ω. Assuming the intensity modulator works at the quadrature point, the incident light can then be decomposed into a series of orders

$$a_{\mathrm{in}} = \sqrt{a_0(0)}\left(\frac{i}{\sqrt{2}} + \frac{1}{\sqrt{2}}\sum_n J_n(\beta_{\mathrm{IM}})e^{-in\Omega t}\right), \tag{S26}$$

where β_{IM} is the intensity modulation depth determined by the RF signal amplitude we dial into our commercial intensity modulator. Thus, the desired beatnote is directly produced from the ±1 sidebands, resulting in a local phonon field with strength $b_n = -g^*\chi_{\mathrm{b,n}}(\Omega)J_1(\beta_{\mathrm{IM}})\left|a_0(0)\right|^2$ at the n-th active region. The distinct microwave output is then given by

$$P_{\mathrm{RF,n}}^{\mathrm{out}}(\Omega) = \frac{\Omega}{\omega_0}\eta_{\mathrm{em,n}}G_{\mathrm{B,n}}J_1^2(\beta_{\mathrm{IM}})P_0^2L\frac{(\Gamma_n/2)^2}{(\Omega-\Omega_n)^2+(\Gamma_n/2)^2}, \tag{S27}$$

which shows adjustable acoustic responses and microwave readouts at distinct frequencies Ω_n with varying bandwidths Γ_n.

According to eq. (S23), the phase modulation stimulated by the acousto-optic interaction in the n-th active region is then given as

$$\tilde{a}(z,t) = \tilde{a}_{\mathrm{in}}\left(t - \frac{z}{v_{\mathrm{g}}}\right)\exp\left[-i\frac{2g|b_n|L}{v_{\mathrm{g}}}\cos(\Omega_n t)\right]. \tag{S28}$$

3. Microwave channelization

When the system features multiple active segments, the new Hamiltonian is described as

$$\mathcal{H} = \int \mathrm{d}z a^\dagger(z,t)\mathcal{L}_a a(z,t) + \sum_n\int_{z_{n-1}}^{z_n}\mathrm{d}z b_n^\dagger(z,t)\mathcal{L}_b b_n(z,t) + g\sum_n\int_{z_{n-1}}^{z_n}\mathrm{d}z a^\dagger(z,t)a(z,t)\left[b_n(z,t)+b_n^\dagger(z,t)\right], \tag{S29}$$

where b_n is the phonon operator of the n-th region, ranging from z_{n-1} to z_n, and $z_0 = 0$. For each segment, eq. (S22) and (S23) still hold, and the optical envelope output from each individual segment can be described as a function of the input to that segment, given as

$$\tilde{a}(z_n,t) = \tilde{a}_{n,\mathrm{in}}\left(t - \frac{z_n - z_{n-1}}{v_{\mathrm{g}}}\right)\exp\left\{-i2g\int_{z_{n-1}}^{z_n}\mathrm{d}z'\,\mathrm{Re}\left[\tilde{b}_n\left(z', t - \frac{z_n - z'}{v_{\mathrm{g}}}\right)\right]\right\}, \tag{S30}$$

where the input to n-th segment $\tilde{a}_{n,\mathrm{in}}(t)$ is the output of the $(n-1)$-th segment, i.e. $\tilde{a}_{n,\mathrm{in}}(t) = \tilde{a}(z = z_{n-1}, t)$. Hence the final output of the system can be obtained using the recursion method

$$\tilde{a}(z,t) = \tilde{a}_{\mathrm{in}}\left(t - \frac{z}{v_{\mathrm{g}}}\right)\exp\left\{-i2g\sum_{n}\int_{z_{n-1}}^{z_n}\mathrm{d}z'\,\mathrm{Re}\left[\tilde{b}_n\left(z', t - \frac{z_n - z'}{v_{\mathrm{g}}}\right)\right]\right\}, \tag{S31}$$

where each segment introduces a unique phase modulation determined by the acoustic properties of that segment, resulting in a constant optical envelope throughout the entire system. When all the active segments are of the same length L, we arrive at the output field

$$\tilde{a}(z,t) = \tilde{a}_{\mathrm{in}}\left(t - \frac{z}{v_{\mathrm{g}}}\right)\exp\left[-i\sum_{n}\beta_n\cos(\Omega_n t)\right], \tag{S32}$$

where $\beta_n = \frac{2g|b_n|L}{v_{\mathrm{g}}}$ is the modulation depth of the n-th region.

2. DESIGN IMPACTS ON DEVICE PERFORMANCE

A. Electromechanical transduction

The electromechanical transduction efficiency, $\eta_{\mathrm{em}} = \eta_{\mathrm{e}}\eta_{\mathrm{m}}$, is determined by two factors, the microwave extinction η_{e} and the target acoustic mode external coupling rate η_{m}. Here we compare and analyze η_{em} across three devices with different numbers of IDT teeth, but the same sets of acoustic eigenmodes, and summarize the key considerations for improving electromechanical transduction when designing electrically interfaced Brillouin-active waveguides.

In our experiment, electromechanical transduction can be directly characterized by the microwave reflection and transmission of the two-IDT system, expressed as $\eta_{\mathrm{e}} = 1 - |S_{11}|^2$ and $\eta_{\mathrm{em}} = |S_{21}|$. Fig. S1 shows the four S-parameter measurements from Device 1, Device 2, and Device 3, which are three different devices with 7, 5, and 3 sets of IDT teeth, respectively, but with the same IDT to phononic crystal distance. The identical IDT to phononic crystal distance results in these three devices featuring the same sets of high-Q acoustic eigenmodes, namely A and B discussed in the main text. This is confirmed in our measurements, where all the S-parameters reveal two resonances at 3.53 GHz and 3.63 GHz. However, these three devices exhibit very different microwave extinction values, indicating varying capabilities of coupling microwave power into the system: the more IDT teeth a device has, the better the impedance matching to a standard 50 Ω input impedance of the RF probe used in the experiment, and the greater the efficiency of coupling microwave power into the system. Additionally, these three devices also display significantly different target acoustic mode external coupling rates, calculated as $\eta_{\mathrm{m}} = \eta_{\mathrm{em}}/\eta_{\mathrm{e}}$. We find that the more IDT teeth a device has, the more well-defined the acoustic drive will be, and as a result, the better η_{m} becomes. In summary, a higher number of IDT teeth in a device leads to more efficient electromechanical transduction.

It should also be noted that the microwave reflections from two IDTs within a single device are not completely identical, i.e., $|S_{11}| \neq |S_{22}|$. However, the variation is within 1%, suggesting that the two IDTs are relatively similar. This discrepancy can be attributed to several factors, including variations in probes, differences in fabrication between the two IDTs, and variations in contact between the two probe-IDT interfaces. To address this variation, we assume the microwave extinction as the geometric mean of the two IDT measurements, given as $\eta_{\mathrm{e}} = \sqrt{\eta_{\mathrm{e},1}\eta_{\mathrm{e},2}}$ in our experiment.

B. Brillouin gain

The Brillouin gain, $G_{\mathrm{B}} = 4g^2/(v_{\mathrm{g}}^2\Gamma_0\hbar\omega_0)$, is determined by two factors, the acousto-optic coupling rate g, and the acoustic loss rate Γ_0. By comparing and analyzing the results of the three devices presented in Fig. S2, we can also identify key considerations for improving the Brillouin gain when designing electrically interfaced Brillouin-active waveguides.

We begin by studying the acousto-optical coupling rate, g, of three devices using COMSOL simulations, which is calculated as

$$g = \frac{1}{\epsilon_0}\sqrt{\frac{\omega_1}{2}}\sqrt{\frac{\omega_2}{2}}\sqrt{\frac{\hbar\Omega_0}{2}}\int\mathrm{d}\mathbf{r}_\perp\left(D^i(\mathbf{r}_\perp)\right)^* D^j(\mathbf{r}_\perp)\,p^{ijkl}(\mathbf{r}_\perp)\,\frac{\partial u_0^k(\mathbf{r}_\perp)}{\partial r^l}, \tag{S33}$$

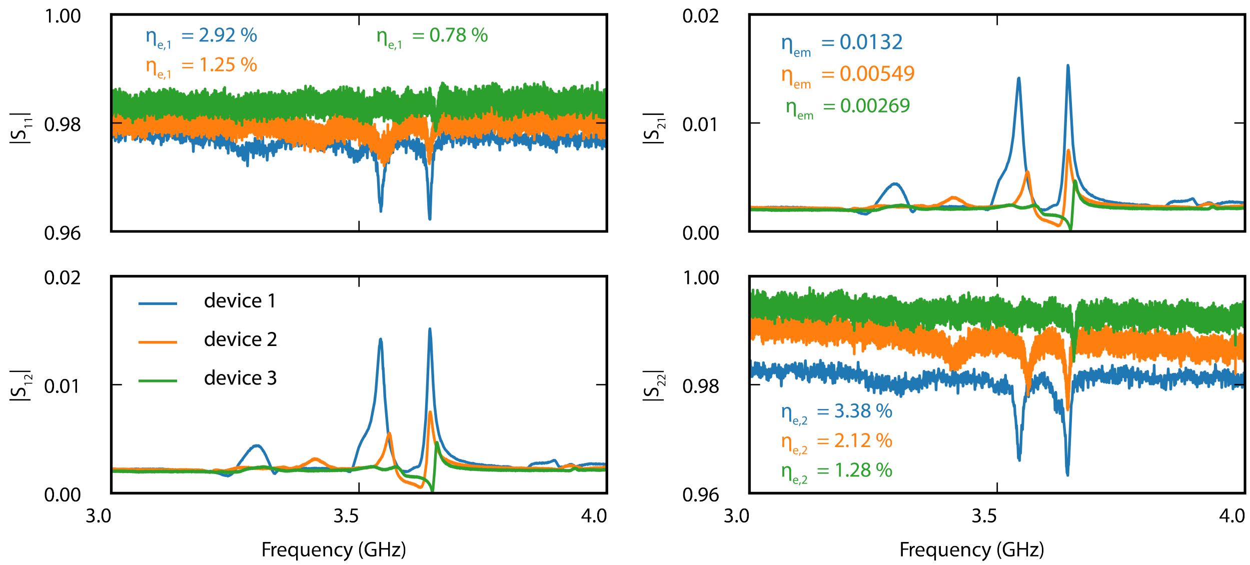

FIG. S1. **The electromechanical transduction evaluation.** The key parameters to determine electromechanical transduction, η_{em} and η_{e}, can be directly derived from the microwave S-parameter measurements. Here we analyze and compare the performance of Device 1 (blue), Device 2 (orange), and Device 3 (green).

where p^{ijkl} is the photoelastic tensor of silicon; D is the electric displacement field of the optical mode, and u is the displacement field of acoustic mode driven by the IDT. Here we follow [6] and use the values $(p_{11}, p_{12}, p_{44}) = (-0.094, 0.017, -0.051)$ for photoelastic coefficients of silicon. The simulation result is presented in Fig. S2a, with the electromechanical resonant point corresponding to mode A marked in circles. We notice that the acousto-optic overlap in Device 1 (blue) is much lower than Device 2 (orange) and Device 3 (green), due to the dilution of the acoustic mode energy over a much larger membrane. We have also observed a mismatch between the frequency for the optimum acousto-optic coupling rate and the electromechanical resonant mode A for Device 1, whereas Devices 2 and 3 are well aligned. This results in Devices 2 and 3 having a significantly larger Brillouin gain compared to Device 1.

We should note that the acousto-optical coupling rate g does not reduce to zero for all devices near the frequency of mode B, despite a noticeable dip. This is because the acoustic modes driven by the IDTs are not limited to the eigenmode mode B; rather, all the excited modes hybridize into a complex mode profile that is not perfectly anti-symmetric. Consequently, the overall integral remains non-zero, which is consistent with our measurement results in Fig. 3b of main text.

The acoustic Q-factor is another factor that affects the Brillouin gain and is proportional to it. As shown in Fig. 5d, increasing the number of metal teeth in the acoustic membrane significantly increases the acoustic loss, which in turn deteriorates the acoustic Q-factor. To determine the impact of these factors on the Brillouin gain for each device, we combined the simulated values of g with the measured acoustic loss rate, Γ_0, to derive theoretical predictions for the Brillouin gain. Our calculations yielded a simulated G_{B} of 91.14 $\mathrm{W^{-1}{\cdot}m^{-1}}$ for Device 1, 271.95 $\mathrm{W^{-1}{\cdot}m^{-1}}$ for Device 2, and 364.24 $\mathrm{W^{-1}{\cdot}m^{-1}}$ for Device 3.

We verify our simulations with the dual-drive setup to measure stimulated Brillouin processes. As illustrated in Fig. 4a, both optical drives are set to the same power level, $P_0 = P_{-1}$. In this experiment, the transduced microwave power is directly proportional to the square of optical input power, as given by $P_{\mathrm{RF}}^{\mathrm{out}}/P_0^2 = \eta_{\mathrm{em}} G_{\mathrm{B}} L \Omega_0/(2\omega_0)$. Fig. S2b presents our measurements of transduced microwave power across three devices as a function of optical input power P_0. Among the three devices, Device 3 (green) exhibits the lowest optical-to-microwave conversion rate due to its unsatisfactory electromechanical transduction efficiency. In contrast, Device 1 (blue) and 2 (green) show comparable performance, with Device 1 having higher electromechanical transduction but lower Brillouin gain, and Device 2 having lower electromechanical transduction but higher Brillouin gain. We extracted the actual Brillouin gain G_{B} values from the linear fits with a slope equal to 2 (black). These values are 27.45 $\mathrm{W^{-1}{\cdot}m^{-1}}$ for Device 1, 66.84 $\mathrm{W^{-1}{\cdot}m^{-1}}$ for Device 2, and 50.64 $\mathrm{W^{-1}{\cdot}m^{-1}}$ for Device 3. The extracted Brillouin gain values were at least a factor of 4 smaller than our simulated values, indicating significant potential for improving the design of future electrically interfaced Brillouin-active waveguides. Several factors contribute to the discrepancy in the extracted gain values, including misalignment between the optimal electromechanical resonance and acoustic modes, which leads to suboptimal acousto-optical

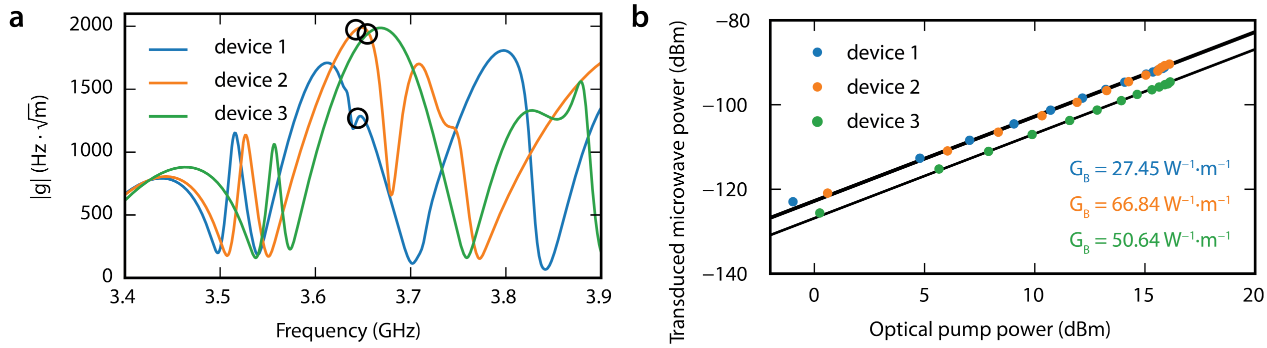

FIG. S2. **The acousto-optical coupling evaluation.** **a**, Simulated acousto-optical coupling rate g as a function of frequency for Device 1, Device 2, and Device 3. The electromechanical resonance, mode A, is marked in a black circle for each of the devices. **b**, The optical-to-microwave conversion effciency meaurements across three devices. The measurements are conducted through a dual-drive experimental setup as illustrated in Fig. 4a.

overlaps, fabrication imperfections resulting in imperfect overlaps, and the reduced photoelastic constants of strained silicon.

C. The interaction length

The selection of the interaction length, L, involves balancing the tradeoff between the higher conversion efficiency associated with longer interaction lengths and the combined benefits of better phase matching, lower optical propagation loss, and improved IDT impedance matching associated with shorter interaction lengths. With all these factors taken into consideration, the quantum efficiency η of bidirectional microwave-to-optical conversion for longer interaction lengths can be described by

$$\eta = \frac{1}{2}\eta_{\mathrm{em}}(L)G_{\mathrm{B}}P_0 e^{-\alpha L}L\mathrm{sinc}^2(\Delta q L/2), \tag{S34}$$

where $\mathrm{sinc}^2(\Delta q L/2)$ accounts for the phase mismatch of the device. $P_0 e^{-\alpha L}$ describes the optical power decay caused by optical propagation loss, and $\eta_{\mathrm{em}}(L)$ describes the dependency of the electromechanical coupling rate on the interaction length. Each factor is discussed in detail below:

- **Optical loss**. The optical loss of the system was evaluated based on our previous measurements in [7], which determined the optical mode propagation loss to be $\alpha = 7.00\ \mathrm{m}^{-1}$. This value corresponds to a negligible optical propagation loss of -4.86×10^{-3} dB in our current design, leading us to omit its discussion in the main text.

- **Phase-mismatch**. According to the phase-matching diagram in Fig. 1d, the wavevector-mismatch was calculated to be $\Delta q = \Omega_0/v_{\mathrm{g}} = 43.75\ \mathrm{m}^{-1}$. This suggests a negligible phase-mismatch loss of -1.75×10^{-4} dB for the current design.

- **IDT impedance mismatch**. The IDT impedance is dependent on the IDT aperture. If we continue using the current IDT design, the aperture needs to be expanded as the interaction length increases. Specifically, the electrical admittance of the transducer is affected, primarily altering the imaginary part of the admittance due to changes in static capacitance, while the real part remains almost constant (See SI Sec. 3 eq. S35, S36). This modification in admittance results in a change in the microwave reflection $|S_{11}|$ of the IDT, consequently affecting the electromechanical coupling rate $\eta_{\mathrm{em}}(L) = \left[1 - |S_{11}(L)|^2\right]\eta_{\mathrm{m}}$.

Based on the previous discussions, we have calculated the variation in conversion efficiency η as a function of the interaction length, relative to the current device. The results of this calculation are summarized in Fig. S3a. We predict that the maximum net gain can be achieved by extending the device length by 23 times(from the current 160 µm to 3.69 mm). This extension is expected to result in an optical propagation loss of -0.112 dB, a phase-mismatch loss of -0.094 dB, and an IDT impedance mismatch loss of -2.607 dB. Despite these losses, the overall quantum efficiency of bidirectional microwave-to-optical transduction could still be improved by 10.825 dB. This calculation also demonstrates the feasibility of achieving more than 100 microwave output channels for microwave

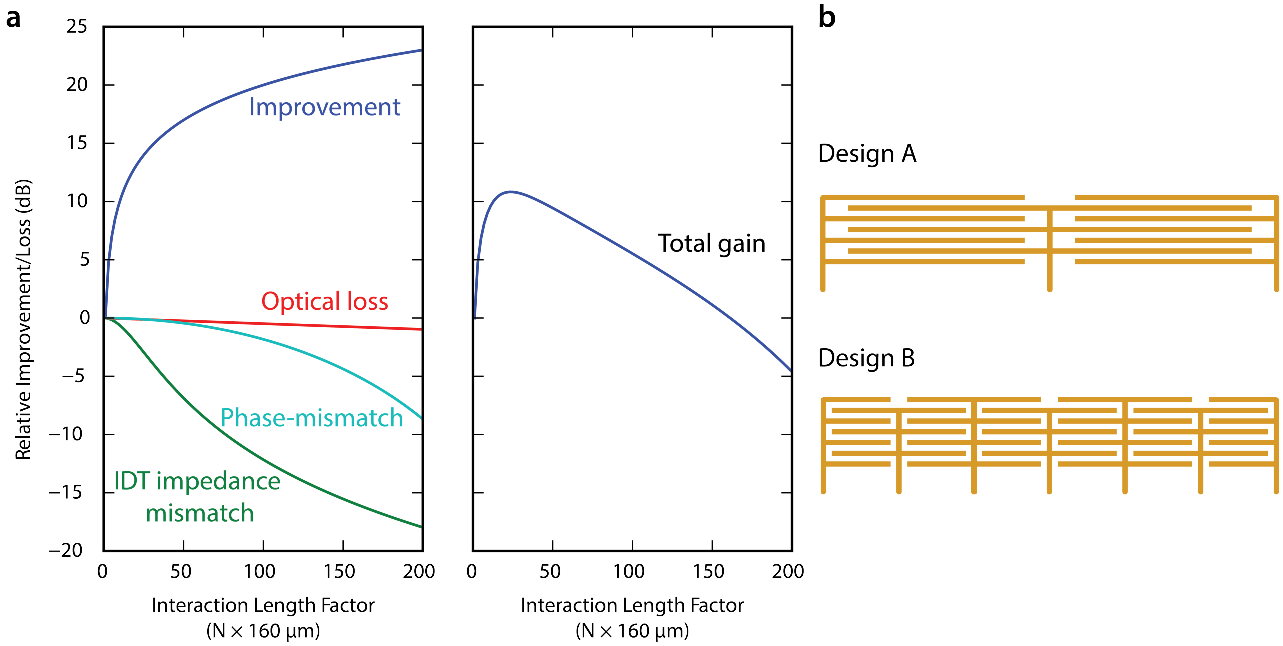

FIG. S3. **The interaction length's impact on device's performance.** **a**, The improvement or loss in conversion efficiency relative to the device 1. We calculate the improvement, the optical propagation loss, the phase-mismatch loss, and the IDT impedance mismatch loss as functions of the extended interaction length, as shown in the left graph. The right graph displays the total net gain resulting from elongating the interaction length, incorporating all these factors. **b**, Two IDT designs for devices with long interaction lengths.

photonic channelization, which would only incur a reasonable total loss of -2.316 dB (in this scenario, the IDT impedance remains unchanged).

It is important to note that IDT impedance matching does not necessarily deteriorate with improvements to the IDT design. As demonstrated in Fig. S3b, the IDT aperture can remain consistent in each section if we employ design B instead of design A (the current design). This indicates that our estimates of conversion efficiency improvement have been conservative. Further discussions on improving the IDT design, however, fall beyond the scope of this paper.

3. RESONANT ENHANCEMENT OF ELECTROMECHANICAL TRANSDUCTION

Our device demonstrates significant electro-mechanical and acousto-optic responses, despite the large impedance mismatch from the standard input impedance of 50 Ω and the presence of less than 10 IDT teeth. This significant enhancement is achieved through the acoustic resonance that we designed into the system. In this section, we study and quantify the electromechanical transduction enhancement resulting from the acoustic resonance by analyzing the admittance of the electromechanical transducer.

The admittance is obtained from the microwave S_{11} measurement of Device 1. According to the Butterworth–Van Dyke model [8], the total electrical admittance of the transducer is given as

$$Y = i\Omega C_s + G(\Omega) + iB(\Omega). \tag{S35}$$

Here C_s is the static capacitance, $G(\Omega)$ and $B(\Omega)$ are the conductance and the susceptance as a function of RF frequency Ω. For a transducer with N finger pairs, the static capacitance is given as:

$$C_s = N w_T(\epsilon_0 + \epsilon_p), \tag{S36}$$

where w_T is the transducer width (aperture) and ϵ_p is the effective permittivity of the piezoelectric material. In our system, $N = 3.5$, $w_T = 160$ μm, and the AlN permittivity $\epsilon_p \approx 9\epsilon_0$, which leads to the static cpacitance of 0.050 pF. This agrees with the off-resonant fitting of the imaginary admittance (the black line in Fig. S4a), which gives $C_s = 0.036$ pF.

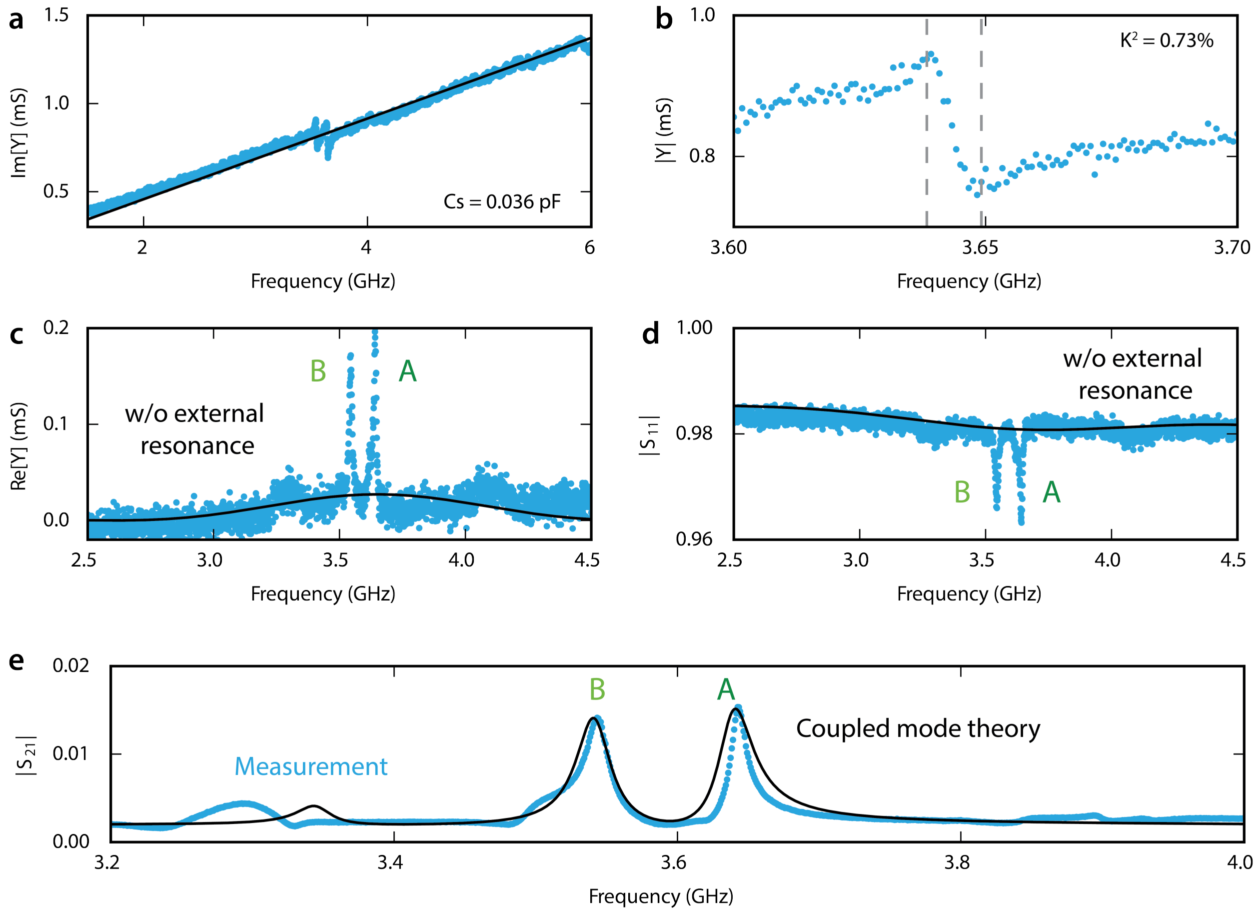

FIG. S4. **The electrical properties of IDT 1 in device 1.** **a**, The imaginary part of the transducer admittance reveals a static capacitance of $C_s = 0.036$ pF, which aligns well with our theoretical calculation of 0.0050 pF. **b**, The absolute value of transducer admittance exhibits a k^2_{eff} of 0.73%, in agreement with the COMSOL simulated value of 1.03%. **c**, We compared the real part of the transducer admittance obtained from measurement (blue) with the theoretical calculation from BVD model (black). The difference between these two curves reveals the resonant enhancement resulting from the acoustic resonances in the device. **d**, We compared the RF reflection $|S_{11}|$ from measurement (blue) with the theoretical calculation from BVD model (black). **e**, The microwave transmission $|S_{21}|$ obtained from measurement (blue) and the coupled mode theory (black).

The radiation conductance $G(\Omega)$ and the motional susceptance $B(\Omega)$ are predicted by the reflection-free impulse response model (IRM) [9] as

$$G(\Omega) = G_0 \mathrm{sinc}^2 x, \;\; B(\Omega) = G_0 \left(\frac{\sin 2x - 2x}{2x^2} \right). \tag{S37}$$

where $x \equiv N\pi \frac{\Omega - \Omega_0}{\Omega_0}$. The peak conductance is determined by $G_0 = 8\Omega_0/(2\pi) k^2_{\mathrm{eff}} C_s N$, where k^2_{eff} is the electromechanical coupling coefficient. For a piezoelectric resonator with resonance frequency Ω_r and antiresonance frequency Ω_a (marked as the dashed lines in Fig. S4b), the electromechanical coupling coefficient is calculated as [8]

$$k^2_{\mathrm{eff}} = \frac{\pi^2}{4} \left(1 - \frac{\Omega_r}{\Omega_a} \right). \tag{S38}$$

According to our measurement in Fig. S4b, $k^2_{\mathrm{eff}} = 0.73\%$. We implemented a similar calculation in COMSOL Multiphysics through the acoustic eigenmode simulation using open (free) and short (metalized) boundary conditions, which consistently gives $k^2_{\mathrm{eff}} = 1.03\%$.

Based on the static capacitance C_s and the electromechanical coupling coefficient k^2_{eff} that we obtained from Fig. S4a and b, the real part of the admittance is calculated using eq. (S35, S37) as the black line in Fig. S4c. The presence of multiple external acoustic resonances significantly increases the 'effective conductance' when the transducer is

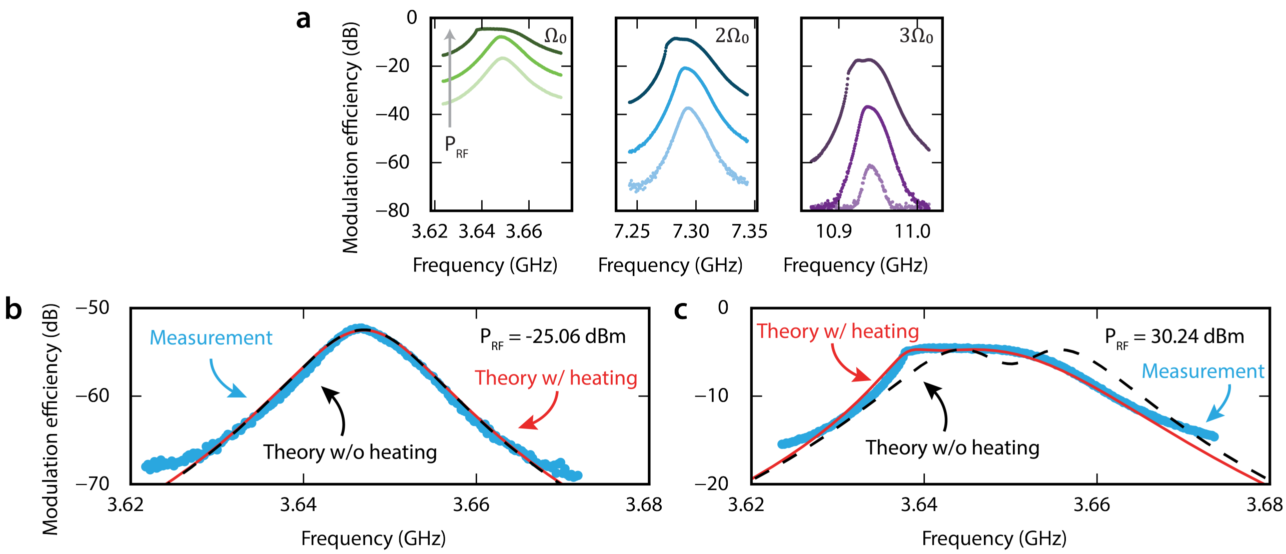

FIG. S5. **The thermal shifting of acoustic resonance under large microwave drive.** **a**, The scattering efficiency of the first three sidebands in the electrically driven acousto-optic phase modulation measurement. The scattering spectrum of each sideband was obtained at three different RF power levels — 10.06 dBm, 20.12 dBm, and 30.24 dBm — indicated by lighter to darker colors, respectively. **b, c**, We introduce two theoretical models to analyze the thermal behavior of the system: the black dashed line represents a model without considering frequency shifts, and the red solid line shows a model derived in eq. (S42) that describes thermal shifting. At low RF drive (**b**), the two models yield identical results and agree well with the measurements (blue), indicating negligible thermal heating. However, at high RF drive (**c**), the resonant frequency is red-shifted, resulting in a flattened spectrum. From the fitting, we extract a thermal heating coefficient of -260 MHz/W, which implies a maximum frequency shift of 8.27 MHz while sweeping frequency at this microwave input power. The system exhibits significant deviation from the ideal model, represented by the black solid line, with the absence of first sideband saturation.

operated on resonance, as denoted by the blue data points in Fig. S4c. For resonance A that we highlighted in Fig. 2, the conductance is improved by a factor of 7 compared with the BVD model without external resonances, resulting in a much better match to the impedance of the standard 50 Ω RF probe. Using the corresponding admittance to calculate the microwave reflection coefficient $|S_{11}|$ and comparing it to the measurement in Fig. S4d, we found that the microwave extinction η_e has improved by approximately four times due to the acoustic resonance.

We developed a simplified model using coupled mode theory to explain the resonant enhancement resulting from the acoustic resonances observed in the system, as depicted in Fig. S4e. In our model, we assume a series of high-Q mechanical modes are present in our system, with each mode separated by the FSR determined by the sound velocity and acoustic membrane width. The dynamics of each mode, b_α, can be described using input-output theory,

$$\dot{b}_\alpha = -i\Omega_\alpha b_\alpha - \frac{\Gamma_\alpha}{2} b_\alpha + \sum_{\alpha'} i\mu_{\alpha\alpha'} b_{\alpha'} + \sqrt{\kappa_\alpha(\Omega)} S_{\mathrm{in}};\ s_{\mathrm{out}} = \sum_\alpha \sqrt{\kappa_\alpha(\Omega)} b_\alpha. \tag{S39}$$

Here, Ω_α and Γ_α describe the resonant frequency and dissipation rate of each acoustic mode, respectively. $\kappa_\alpha(\Omega) = 4Y_0Y(\Omega)/(Y_0 + Y(\Omega))$ describes the electric extrinsic coupling rate of the acoustic resonance, which depends on the admittance calculated in the black curve of Fig. S4c. The inclusion of metal gratings and multiple acoustic reflectors in the device leads to undesired coupling, $\mu_{\alpha\alpha'}$, between adjacent high-Q modes, b_α and $b_{\alpha'}$, resulting in uneven microwave transmission and varying acoustic linewidths for each distinct acoustic mode. Our theoretical predictions (black) align well with the experimental measurements (blue), indicating that the acoustic mode frequency can be effectively controlled through the acoustic membrane design. This can be achieved by adjusting the acoustic membrane width to alter the signal FSR or by designing the reflectors' position to regulate the intermodal coupling.

4. THERMAL BISTABILITY UNDER LARGE MICROWAVE DRIVE

We observe some spectral distortion under large microwave drive power in our measurement of electrically driven acousto-optic phase modulation. Here we present the scattering efficiency of the first three sidebands in Fig. S5a, measured using Device 1, following the experimental setup shown in Fig. 2b. The scattering efficiency produced over

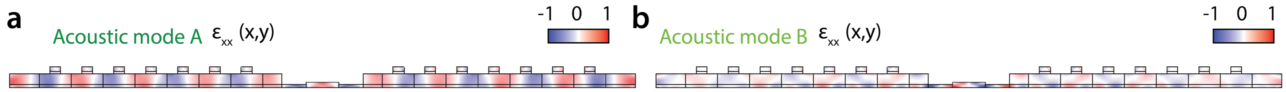

FIG. S6. **The full acoustic profiles (xx component of the strain) of the acoustic eigenmodes A (a) and B (b).**

a range of drive frequencies is shown for three different RF powers, 10.06 dBm, 20.12 dBm, and 30.24 dBm, which are depicted from lighter to darker colors. At low RF power, each optical tone exhibits a Lorentzian-like frequency-dependent modulation amplitude due to the presence of the phonon resonance. As the RF power increases, the phase modulation gradually gets saturated, and the measured acoustic waveshape gets distorted and thermally shifted from the standard Lorentzian shape. In this section, we offer a comprehensive analysis of this thermal shifting, presenting evidence from experimental results and theoretical derivations.

To solve this problem, we make several assumptions. First, we assume that all the on-chip microwave power that is not converted into acoustic power is instead absorbed as heat, which is determined as

$$P_{\mathrm{abs}}(\Omega) = \eta_{\mathrm{e}} P_{\mathrm{RF}}^{\mathrm{in}} - P_{\mathrm{a}} = \left(1 - \frac{\xi}{(\Omega - \Omega_0 - \delta\Omega)^2 + \frac{\Gamma_0^2}{4}}\right) \eta_{\mathrm{e}}(\Omega) P_{\mathrm{RF}}^{\mathrm{in}}, \tag{S40}$$

where $\delta\Omega$ is the frequency shift of the acoustic resonance. It is important to note that the microwave extinction $\eta_{\mathrm{e}}(\Omega)$ is a function of the incident microwave frequency and should also incorporate the thermal shift of the acoustic resonance as

$$\eta_{\mathrm{e}}(\Omega) = \eta_{\mathrm{e}}(\Omega_0) \frac{\frac{\Gamma_0^2}{4}}{(\Omega - \Omega_0 - \delta\Omega)^2 + \frac{\Gamma_0^2}{4}}. \tag{S41}$$

Secondly, we assume that, to the first order, the frequency shift of the acoustic resonance is proportional to the absorbed power, written as $\delta\Omega = c_{\mathrm{heat}} P_{\mathrm{abs}}(\Omega)$, where c_{heat} is the heating coefficient with unit Hz/W. As a result, the absorption power P_{abs} can be solved as an expression that is dependent on the detuned frequency $\Omega - \Omega_0$ and the heating coefficient c_{heat}. If we plug the expression of the P_{abs} back into the phonon amplitude, the modulation efficiency of the 1st sideband can then be expressed by the absorption power P_{abs} as

$$\frac{|a_1|^2}{|a_0|^2} = \left| J_1 \left(\frac{2gL}{v_{\mathrm{g}}} \sqrt{\frac{\xi \eta_{\mathrm{e}}(\Omega)}{(\Omega - \Omega_0 - c_{\mathrm{heat}} P_{\mathrm{abs}})^2 + \frac{\Gamma_0^2}{4}} \frac{P_{\mathrm{RF}}^{\mathrm{in}}}{\hbar \Omega L}} \right) \right|^2. \tag{S42}$$

In Fig.S5, we present our theoretical calculations alongside the measurements of the first sideband modulation spectra. We introduce two theoretical models: the dashed black line represents the model without frequency shifting from thermal heating, and the solid red line corresponds to the theoretical fitting derived in eq. (S42), accounting for frequency shifts due to thermal heating. We observe that at low microwave drive ($P_{\mathrm{RF}}^{\mathrm{in}}$ = -25.06 dBm), where thermal shifting is negligible, the two theoretical models converge into an identical trace that agrees well with the experimental measurements. However, at high microwave drive power ($P_{\mathrm{RF}}^{\mathrm{in}}$ = 30.24 dBm), where thermal shifting becomes dominant in the experiment, we observe a significant red-shifting of the resonant frequency of the phonon modes in the red line, which is in good agreement with the flattened measured spectra. According to our fitting, we extract a linewidth broadening to 20 MHz and a thermal shifting parameter c_{heat} of 260 MHz/W. This indicates that at this microwave drive input, the maximum thermal absorption while sweeping the frequency is about 31.8 mW, which corresponds to a frequency shift of 8.27 MHz. Our model effectively explains why our system does not exhibit phase modulation saturation at high microwave power, as highlighted by the contrast between the resonant dip in the ideal model without thermal heating (dashed line) and the actual system. At present, our thermal model does not adequately fit the higher-order sideband modulation spectra. We hypothesize that this may be due to the intricate behavior exhibited by the higher-order sidebands, resulting from a combination of effects, such as IDT overtones, the presence of unwanted acoustic modes in the system, and the heating effect. However, a more comprehensive understanding of this issue necessitates further investigation.

5. THE ACOUSTIC EIGENMODES

In the insets of Fig. 2d, we present the zoomed-in ϵ_{xx} profiles for acoustic eigenmodes A and B. For a comprehensive analysis, this section includes the full strain profiles of mode A in Fig. S6a and mode B in Fig. S6b. Both modes have been normalized to the maximum values of their own strain profiles. These modes were simulated using the eigenmode simulations of the COMSOL Multiphysics Solid Mechanics Package.

6. COMPARING OUR SYSTEM WITH THE PHOTODIODES

Direct photodetection has been the primary option for optical-to-electrical conversion for decades. Here, we list the advantages and key differences of our device over traditional photodiodes for the reader's reference:

1. **Non-destructive vs. Destructive Measurement**: To maximize the responsivity of photodetectors, photons are fully absorbed to excite free carriers, thereby generating fast oscillating photocurrent at microwave frequencies. Consequently, the optical field and the information encoded within it are fully destroyed in single-shot measurements. In contrast, our method involves the optical force generated by the beat note of the optical field, which creates phonons and RF signals without destroying or absorbing photons. Instead, the photons experience a slight redshift in frequency to convert energy into generated phonons, making our measurement a non-destructive microwave photonic measurement: the photon number is preserved in the process and information encoded on the intensity envelop is not altered.

2. **External Classical Gain vs. Passive Operation**: Traditional photodiodes require at least an external voltage source, which pulls and accelerates photon-generated free carriers, providing additional gain to the system. In contrast, our system operates entirely passively, without any need for external classical gain.

3. **Signal Processing Capabilities**: Conventional microwave photonic systems, reliant on photodetectors, often require all microwave signal processing to be conducted in the microwave domain. This requires additional power sources, complex external electrical circuits, transimpedance amplifiers, among other components. Our device offers a unique, stand-alone, all-integrated platform for simultaneous microwave detection and filtering while preserving the information in the optical domain — a function unattainable by a single photodetector.

Due to the features of non-destructive microwave photonic measurements, the all-passive operation, and the narrowband microwave photonic filtering capacity, our device would suit very different application scenarios from the traditional photodiodes, such as remote sensing and optical signal processing.

[1] P. Kharel, R. O. Behunin, W. H. Renninger, and P. T. Rakich, Noise and dynamics in forward brillouin interactions, Physical Review A **93**, 063806 (2016).

[2] J. Sipe and M. Steel, A hamiltonian treatment of stimulated brillouin scattering in nanoscale integrated waveguides, New Journal of Physics **18**, 045004 (2016).

[3] C. Wolff, B. Stiller, B. J. Eggleton, M. J. Steel, and C. G. Poulton, Cascaded forward brillouin scattering to all stokes orders, New Journal of Physics **19**, 023021 (2017).

[4] M. Aspelmeyer, T. J. Kippenberg, and F. Marquardt, Cavity optomechanics, Reviews of Modern Physics **86**, 1391 (2014).

[5] S. Gertler, P. Kharel, E. A. Kittlaus, N. T. Otterstrom, and P. T. Rakich, Shaping nonlinear optical response using nonlocal forward brillouin interactions, New Journal of Physics **22**, 043017 (2020).

[6] D. K. Biegelsen, Photoelastic tensor of silicon and the volume dependence of the average gap, Physical Review Letters **32**, 1196 (1974).

[7] Y. Zhou, F. Ruesink, S. Gertler, H. Cheng, M. Pavlovich, E. Kittlaus, A. L. Starbuck, A. J. Leenheer, A. T. Pomerene, D. C. Trotter, *et al.*, Intermodal strong coupling and wideband, low-loss isolation in silicon, arXiv preprint arXiv:2211.05864 (2022).

[8] D. Royer and E. Dieulesaint, *Elastic waves in solids II: generation, acousto-optic interaction, applications* (Springer Science & Business Media, 1999).

[9] C. S. Hartmann, D. T. Bell, and R. C. Rosenfeld, Impulse model design of acoustic surface-wave filters, IEEE Transactions on Microwave Theory and Techniques **21**, 162 (1973).